Supporting Information

Klein *et al.* 10.1073/pnas.0802286105

SI Text

SI Methods. ***Protein preparations and spin labeling.*** Cysteine mutations for spin labeling sites were introduced into a *Dicty* myosin II gene truncated at residue 762, containing only a single non-reactive Cys at position 655. Mutations were C49T, C312S, C442S, C470V, C599T, and C678S. This Cys-depleted S1dC expresses at very low levels, so A250C was introduced to increase expression for a control mutant used for assessing function (Table S1). Spin labels were IPSL [3-(2-Iodoacetamido)-2,2,5,5-tetramethyl-1-pyrolidinyloxy] or MSL [N-(1-Oxyl-2,2,6,6-tetramethyl-4-piperidinyl)maleimide] (Toronto Research Chemicals, North York, Ontario).

Activity measurements. Functional measurements were performed at 25°C. ATPase activity was detected as the release of inorganic phosphate (1, 2). High-salt Ca/K ATPase activity was measured in a solution containing 0.0125 mg/ml myosin, 10 mM $CaCl_2$, 600 mM KCl, 5 mM ATP, and 50 mM Mops (pH 7.5). Actin-activated ATPase activity was measured as the increase in activity due to the addition of 10 μM rabbit skeletal actin to a solution containing 1 μM myosin, 3.5 mM $MgCl_2$, 10 mM KCl, and 10 mM Mops (pH 7.5). Co-sedimentation binding assays were performed by mixing 200 μM actin and 100 μM myosin in EPR buffer followed by centrifugation at 75,000 rpm to pellet the actoS1dC complexes. Supernatant and pellet samples were analyzed by SDS/PAGE.

CW EPR: Mobility and accessibility. EPR samples contained 100 μM myosin S1dC in EPR buffer. The ADP.V state was formed by addition of 5 mM ADP, followed by 5 mM Na_3VO_4. The actomyosin state was formed by addition of 200 μM F-actin. For accessibility measurements, duplicate samples were prepared, one containing 5 mM ethylenediamine-N,N′-diacetic acid (NiEDDA) as the paramagnetic relaxation agent. EPR was performed on deoxygenated samples at 4°C using a Bruker E500 spectrometer (Billerica, MA) at X-band (9.5 GHz), with modulation frequency 100 kHz and modulation amplitude 2 G. Mobility was measured in gas-permeable Teflon tubes (0.6 mm I.D., 20 μl sample volume) sealed with critoseal, placed into the quartz temperature control dewar inside an SHQ cavity (ER4122 ST). Scan width was 120 G and the microwave power of 2 mW produced ≈40% saturation, with no significant line broadening. Plotted spectra (Fig. 2) were normalized to the double integral. Solvent accessibility was measured by power saturation in gas-permeable TPX tubes containing 4 μl sample in a dielectric resonator (ER4123D). Spectra were acquired for fifteen microwave powers between 0.002 mW and 100 mW; the scan width was reduced to 12 G to capture only the central line.

Order parameters were measured from EPR spectra by simulation and fitting with the software NLSL (Nonlinear Least-Squares Analysis of Slow-Motional EPR Spectra) (3–5). Spectra were simulated for a two-component system, each with its own order parameter (S), correlation time (τ_r), and mole fraction (x_i). Then S was calculated from $S = x_1S_1 + x_2S_2$. The order parameter ranges from 0 to 1, with 1 being maximum restriction of rotational motion.

Spin label accessibility to paramagnetic relaxation agent was measured by EPR power saturation as described previously (6–10). After Gaussian lineshapes were fit to the central line, peak-peak lineheight A was measured at each successive microwave power P, and the data were fitted to

$$A = I\cdot\left[1 + \frac{(2^{1/\epsilon} - 1)\cdot P}{P_{1/2}}\right]^{-\epsilon} \qquad \textbf{[s1]}$$

where $P_{1/2}$ is the value of P at half-saturation, and ε depends on the heterogeneity of line-broadening (6–8). The increase in $P_{1/2}$ due to the presence of paramagnetic relaxation agent ($\Delta P_{1/2}$), divided by central linewidth, is proportional to the accessibility of the site. $\Delta P^{\circ}_{1/2}$ is defined as the accessibility of the most accessible site in the study. Fractional accessibility is defined as the ratio of $\Delta P_{1/2}$ to $\Delta P^{\circ}_{1/2}$; from 0 (least accessible) to 1 (most accessible).

Spin–spin distance measurements. EPR samples for spin-spin distance measurements were the same as in other EPR experiments, as described above, except that the buffer also contained 10% glycerol (vol/vol), and the 100 μl samples were flash-frozen using liquid nitrogen in a 5 mm OD quartz NMR tube (Wilmad glass, Buena NJ) and stored at −80°C until use. CW EPR was performed using the E500 spectrometer at X-band (9.5 GHz) equipped with an SHQ cavity. Spectra were acquired at 200 K under nitrogen gas flow. The modulation amplitude was decreased to 1G and the microwave power to 0.6 mW to avoid broadening by overmodulation or power saturation. The scan width was increased to 200 G to detect broadening in the spectral wings. Pulsed EPR experiments were performed with a Bruker E580 spectrometer (Billerica, MA) at X-band (9.5 GHz) with a Bruker dielectric ring resonator (MD-5) using a 4-pulse DEER (Double Electron Electron Resonance) protocol (11). The $\pi/2$ pulse width was 16 ns, and the ELDOR pulse width was 40–44 ns. The static field was set to the low-field resonance of the nitroxide signal. Temperature was controlled at 65 K during acquisition, which lasted 4–12 h.

Spin–spin distances were determined by fitting the experimental EPR data with simulations assuming a distance distribution function consisting of a sum of Gaussians:

$$p(r) = \sum_{i=1}^{n} x_i g_i(r) \qquad \textbf{[s2]}$$

$$g_i(r) = A\frac{1}{\sigma_i\sqrt{2\pi}}e^{(r-r_i)^2/2\sigma_i^2}. \qquad \textbf{[s3]}$$

The $3n$-1 variable parameters in the fit were x_i (mole fraction), r_i (center distance), and σ_i (standard deviation), where the full width at half maximum, w_i, is given by $w_i = 2\sigma_i\sqrt{\ln 2}$. The number of components n in the best fit was defined as the one for which $n + 1$ produced no further improvement, as defined by the residual plot and by the residual sum of squares. The distribution function (Eq. S3) was convoluted with the Pake pattern (12) to simulate the weighted sum of the dipolar broadening function over the distance distribution (13), and this was used to simulate the EPR data, essentially as described previously for CW EPR (14, 15) and for DEER (16). CW EPR spectra were fit using a Monte Carlo search procedure with laboratory-developed software (WACY, Edmund Howard). DEER background correction, distance determination by Tikhonov regularization, and fits based on Gaussian distance distributions were performed using methods provided in the software DEERAnalysis2006.1 (16, 17). Distances extracted by Tikhonov regularization were consistent with fits based on Gaussian distance distributions. We report the results based on Gaussian distance distributions; because they are more useful for discussing models based on discrete conformational states that are common to different biochemical states. The quality of the

fit was assessed using methods provided in the software DEFit (18, 19).

Computational simulations based on crystal structures. Crystal structures 1FMV, 1VOM and 1W8J were modified to include missing loops and residues using InsightII (Accelrys Inc., San Diego, CA). Native residues were mutated to spin-labeled cysteines using Visual Molecular Dynamics (VMD) (20). Sequence alignment of myosin V and myosin II was performed in VMD to determine corresponding mutation sites in the myosin V structure. We adapted parameters for the IPSL and MSL spin labels from CHARMM19 united atom force fields for spin labels originally obtained through Piotr Fajer (Florida State University). Metropolis Monte Carlo Minimization (MMCM) (21, 22) was used to determine starting points for molecular dynamics (MD) simulations. Langevin MD simulations were performed in CHARMM (23, 24) with the CHARMM19 united atom force field, using the EEF1 implicit solvation model (25) with a friction coefficient of 5 for more efficient conformational sampling (26). Residues beyond 25 Å of the labels were fixed and C^{α} atoms of residues beyond 22 Å were harmonically restrained (0.3 kcal/mol force constant). The temperature was gradually increased in increments of 20K to 300K over 100ps. The protein was then allowed to equilibrate for 0.5 ns by gradually decreasing the force constant on C^{α} atom constraints from 1.0 kcal/mol to 0.3 kcal/mol. In parallel, we performed MD simulations with the C^{α} atoms of backbone residues restrained to preserve the original crystal structure backbone conformation. The parameters are available from the authors upon request.

Simulated mobility, accessibility, and distance. We calculated spin label order parameters from MD trajectories according to the procedure developed previously in this laboratory (27). The order parameter, S, is defined as follows:

$$S = 1.5\langle\cos^2\beta\rangle - 0.5 \qquad \textbf{[s4]}$$

and

$$\langle\cos^2\beta\rangle = \Sigma\cos^2\beta\rho(\beta)\sin\beta d\beta \qquad \textbf{[s5]}$$

where β is the angular deviation from the mode of the orientational distribution of the z axis of the nitroxide over the course of the simulation. The simulated order parameter is compared directly to the experimental order parameter, both parameters ranging from 0 (minimum motional restriction) to 1 (maximum motional restriction). Solvent accessible surface area (SASA) was calculated in VMD for both the unlabeled (native) residue side chain and for the IPSL 5-membered ring for every frame using a 4 Å probe radius to mimic NiEDDA. The average surface area was normalized to the surface area of the native side chain or spin label side chain free in solution and the most fully solvent-exposed site in the study. Simulated accessibility ranges from 0 (minimum accessibility) to 1 (maximum accessibility). Distances between spin label nitroxide oxygen atoms were measured in VMD, binned into 1 Å bins and normalized by area.

SI Results and Discussion. ***Dipolar broadened CW EPR spectral analysis.*** To justify the conclusion that multiple Gaussian distance distributions are required to adequately fit dipolar broadened CW EPR spectra (Fig. 5), we have included fitting parameters for one, two and three Gaussian fits in Table S2. These fits, along with residuals, are plotted in supporting information (SI) Fig. S1. Goodness of fit was assessed by calculating the residual sum of squares (RSS) between the data and simulated fit and also by visual inspection of residuals. We note that it is not possible to achieve flat residuals for all spectra, notably in cases where the predicted distance is less than 0.8 nm (Fig. S2). For these samples isotropic spin exchange contributes to spectral changes that are not accounted for in our model. A four Gaussian fit was performed for the 270:463 *apo* spectrum (not shown) but it did not result in a better fit than using three Gaussians. A third Gaussian visibly improved the fit to the 270:463 *apo* spectrum, but had no significant effect for 416:583 *apo* and the actin-bound spectra (Table S2 and Fig. S1). The major features of the 416:583 ADP.V spectrum are fit by a single component; two components are needed to fit 270:463 ADP.V but the second is only needed at a mole fraction of 0.22 (Table S2 and Fig. S1).

DEER data analysis. For the 537:401 actin-bound DEER sample, the maximum evolution time was limited by the phase memory time (T_m) to just under 1 μs. An evolution time of 1 μs captures one full oscillation due to a distance of 3.6 nm. Although a full oscillation is not required to extract distances greater than 3.6 nm from a 1 μs evolution time, it is prudent to test the sensitivity of the fit quality to changes in the fitting parameters. We varied both the distance distribution center (r) and full width at half maximum (w) for the long distance component of the best fit and calculated the residual between data and simulated fit. Simulated decays corresponding to r $\pm$ 0.3 nm fits the most outlying data points in the region of the decay most sensitive to r for the long distance component (0.1–0.4 μs) (Fig. S3A). The fit is markedly less sensitive to changes in distribution width (simulated decays correspond to 0 nm and 1.8 nm), but widths broader than 1.8 nm are inconsistent with the data near 0.1 μs (Fig. S3B). Thus we conclude that the 537:401 actin-bound DEER decay can only arise from a long distance component centered at 3.7 $\pm$ 0.3 nm with a distribution width of 0.8 $\pm$ 1 nm.

Computational simulations of spin–spin distances in inner/middle cleft. Distance distributions obtained from CW EPR spectra of spin-labeled residue pairs 270:463 and 416:583 (Fig. 5) were directly compared to distances obtained from MD simulations (Fig. S2). Each of the three structural models tested (with restrained C^{α} in pink) produced a single distance distribution in close agreement with one of the three distances resolved by EPR at 270:463 (Fig. S2). This suggests a correspondence between cleft conformation in solution and that in the crystal structure. Releasing C^{α} restraints in the 1FMV and 1W8J simulations did not produce a distance change that would be detected by CW EPR, but for 1VOM, stabilized a spin label conformation that did not agree with any EPR-detected components. At 416:583 computational simulations did not produce resolvable distance distributions corresponding to each of the three structural models, with or without backbone restraints.

1. Lanzetta PA, Alvarez LJ, Reinach PS, Candia OA (1979) An improved assay for nanomole amounts of inorganic phosphate. *Anal Biochem* 100:95–97.
2. Fiske CH (1925) The calorimetric determination of phosphorus. *J Biol Chem* 66:375–400.
3. Budil DE, Lee S, Saxena S, Freed JH (1996) Nonlinear-least-squares analysis of slow-motion EPR spectra in one and two dimensions using a modified Levenberg-Marquardt algorithm. *J Magn Reson A* 120:155–189.
4. Nesmelov YE, Karim CB, Song L, Fajer PG, Thomas DD (2007) Rotational dynamics of phospholamban determined by multifrequency electron paramagnetic resonance. *Biophys J* 93:2805–2812.
5. Nesmelov YE, Agafonov RV, Burr A, Weber RT, Thomas DD (2008) Structure and dynamics of the force generating domain of myosin probed by site-directed spin labeling and multifrequency electron paramagnetic resonance. *Biophys J* 95:247–256.
6. Altenbach C, Froncisz W, Hemker R, McHaourab H, Hubbell WL (2005) Accessibility of nitroxide side chains: Absolute Heisenberg exchange rates from power saturation EPR. *Biophys J* 89:2103–2112.
7. Altenbach C, Marti T, Khorana HG, Hubbell WL (1990) Transmembrane protein structure: spin labeling of bacteriorhodopsin mutants. *Science* 248:1088–1092.
8. Altenbach C, Greenhalgh DA, Khorana HG, Hubbell WL (1994) A collision gradient method to determine the immersion depth of nitroxides in lipid bilayers: Application to spin-labeled mutants of bacteriorhodopsin. *Proc Natl Acad Sci USA* 91:1667–1671.
9. Kirby TL, Karim CB, Thomas DD (2004) Electron paramagnetic resonance reveals a large-scale conformational change in the cytoplasmic domain of phospholamban upon binding to the sarcoplasmic reticulum Ca-ATPase. *Biochemistry* 43:5842–5852.

10. Surek JT, Thomas DD (2008) A paramagnetic molecular voltmeter. *J Magn Reson* 190:7–25.
11. Pannier M, Veit S, Godt A, Jeschke G, Spiess HW (2000) Dead-time free measurement of dipole-dipole interactions between electron spins. *J Magn Reson* 142:331–340.
12. Pake GE (1948) Nuclear resonance absorption in hydrated crystals: Fine structure of the proton line. *J Chem Phys* 16:327–336.
13. Rabenstein MD, Shin YK (1995) Determination of the distance between two spin labels attached to a macromolecule. *Proc Natl Acad Sci USA* 92:8239–8243.
14. Steinhoff HJ, *et al.* (1997) Determination of interspin distances between spin labels attached to insulin: comparison of electron paramagnetic resonance data with the X-ray structure. *Biophys J* 73:3287–3298.
15. Altenbach C, Oh KJ, Trabanino RJ, Hideg K, Hubbell WL (2001) Estimation of inter-residue distances in spin labeled proteins at physiological temperatures: Experimental strategies and practical limitations. *Biochemistry* 40:15471–15482.
16. Jeschke G, Koch A, Jonas U, Godt A (2002) Direct conversion of EPR dipolar time evolution data to distance distributions. *J Magn Reson* 155:72–82.
17. Jeschke G (2002) Distance measurements in the nanometer range by pulse EPR. *Chemphyschem* 3:927–932.
18. Fajer MI, Li H, Yang W, Fajer PG (2007) Mapping electron paramagnetic resonance spin label conformations by the simulated scaling method. *J Am Chem Soc* 129:13840–13846.
19. Fajer PG, Brown L, Song L (2006) *Practical Pulsed Dipolar EPR (DEER)* (Springer, Berlin).
20. Humphrey W, Dalke A, Schulten K (1996) VMD: Visual molecular dynamics. *J Mol Graphics* 14:33–38.
21. Sale K, Sar C, Sharp KA, Hideg K, Fajer PG (2002) Structural determination of spin label immobilization and orientation: A Monte Carlo minimization approach. *J Magn Reson* 156:104–112.
22. Sale K, Song L, Liu YS, Perozo E, Fajer P (2005) Explicit treatment of spin labels in modeling of distance constraints from dipolar EPR and DEER. *J Am Chem Soc* 127:9334–9335.
23. Brooks BR, *et al.* (1983) CHARMM: A program for macromolecular energy, minimization, and dynamics calculations. *J Comput Chem* 4:187–217.
24. MacKerell AD, Jr, *et al.* (1998). in *The Encyclopedia of Computational Chemistry*, eds Schleyer, PvR, *et al.* (Wiley, Chichester, NY), Vol 1, pp 271–277.
25. Lazaridis T, Karplus M (1999) Effective energy function for proteins in solution. *Proteins* 35:133–152.
26. Loncharich RJ, Brooks BR, Pastor RW (1992) Langevin dynamics of peptides: the frictional dependence of isomerization rates of N-acetylalanyl-N′-methylamide. *Biopolymers* 32:523–535.
27. LaConte LE, Voelz V, Nelson W, Enz M, Thomas DD (2002) Molecular dynamics simulation of site-directed spin labeling: Experimental validation in muscle fibers. *Biophys J* 83:1854–1866.
28. Korman VL, Anderson SE, Prochniewicz E, Titus MA, Thomas DD (2006) Structural dynamics of the actin-myosin interface by site-directed spectroscopy. *J Mol Biol* 356:1107–1117.

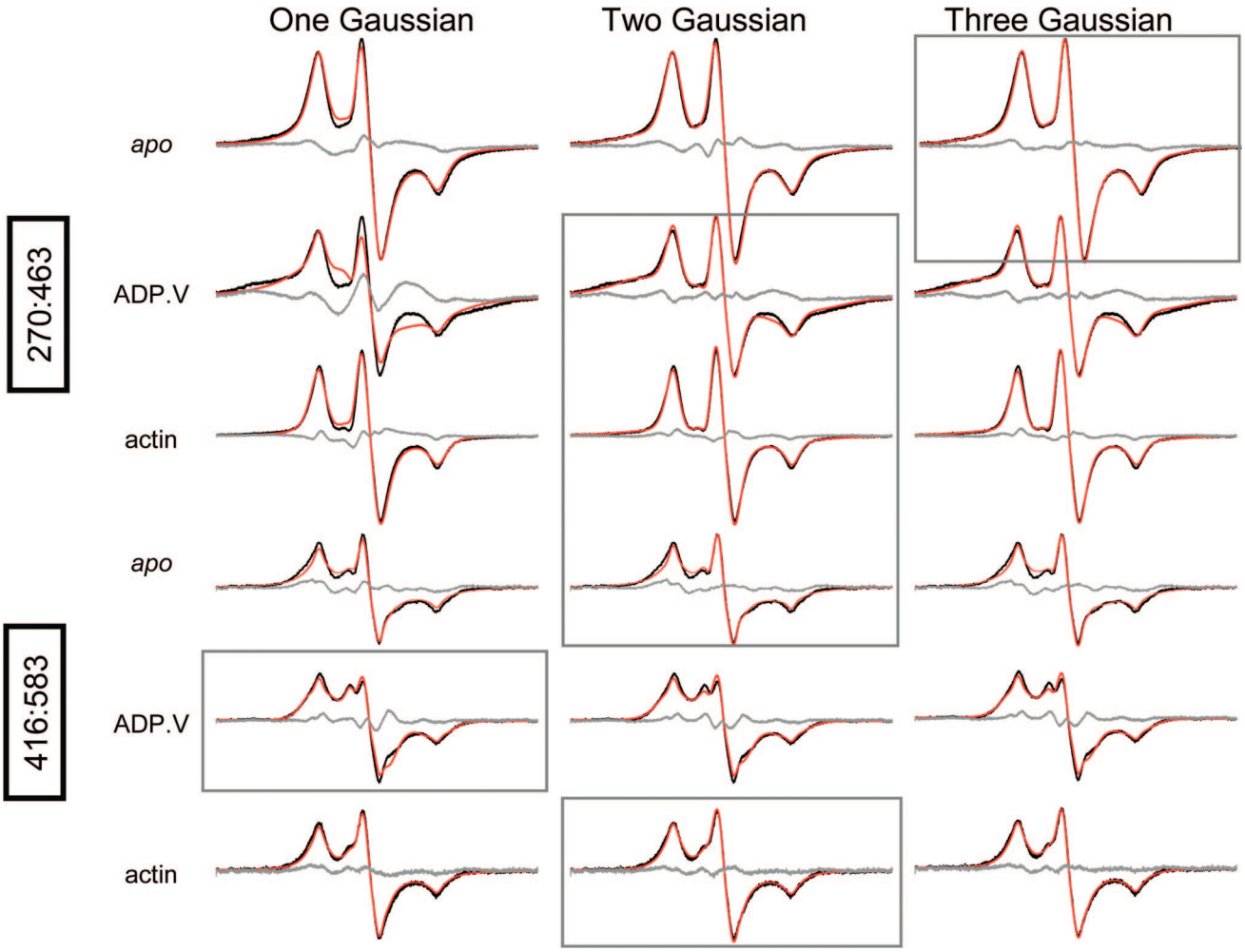

Fig. S1. Best fits to dipolar broadened CW EPR spectra assuming one, two or three Gaussian distance distributions for 270:463 and 416:583. Experimental spectra are black, fits are red, and residuals are gray. The residuals are defined as experiment minus simulated fit. The fit that best represents the data are enclosed by a box. Parameters resulting from fits are shown in Table S2.

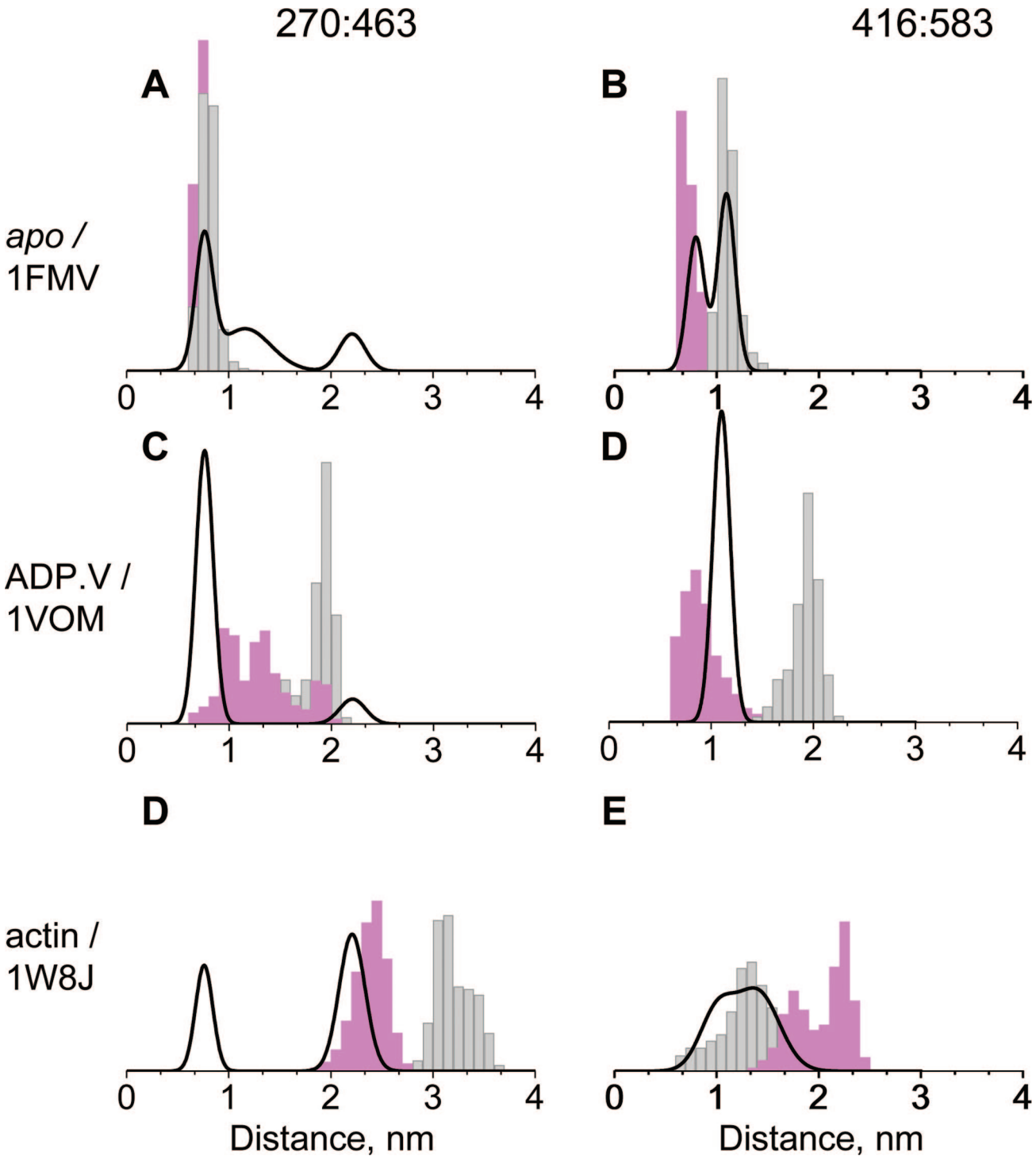

Fig. S2. Overlay of CW EPR distance distributions for 270:463 and 416:583 *apo*, ADP.V and actin bound biochemical states (black curves, from Fig. 5) and distance distributions derived from MD simulations based on crystal structures 1FMV, 1VOM and 1W8J (see Fig. 1). Pink indicates restrained C^{α} atoms. Gray indicates unrestrained C^{α} atoms.

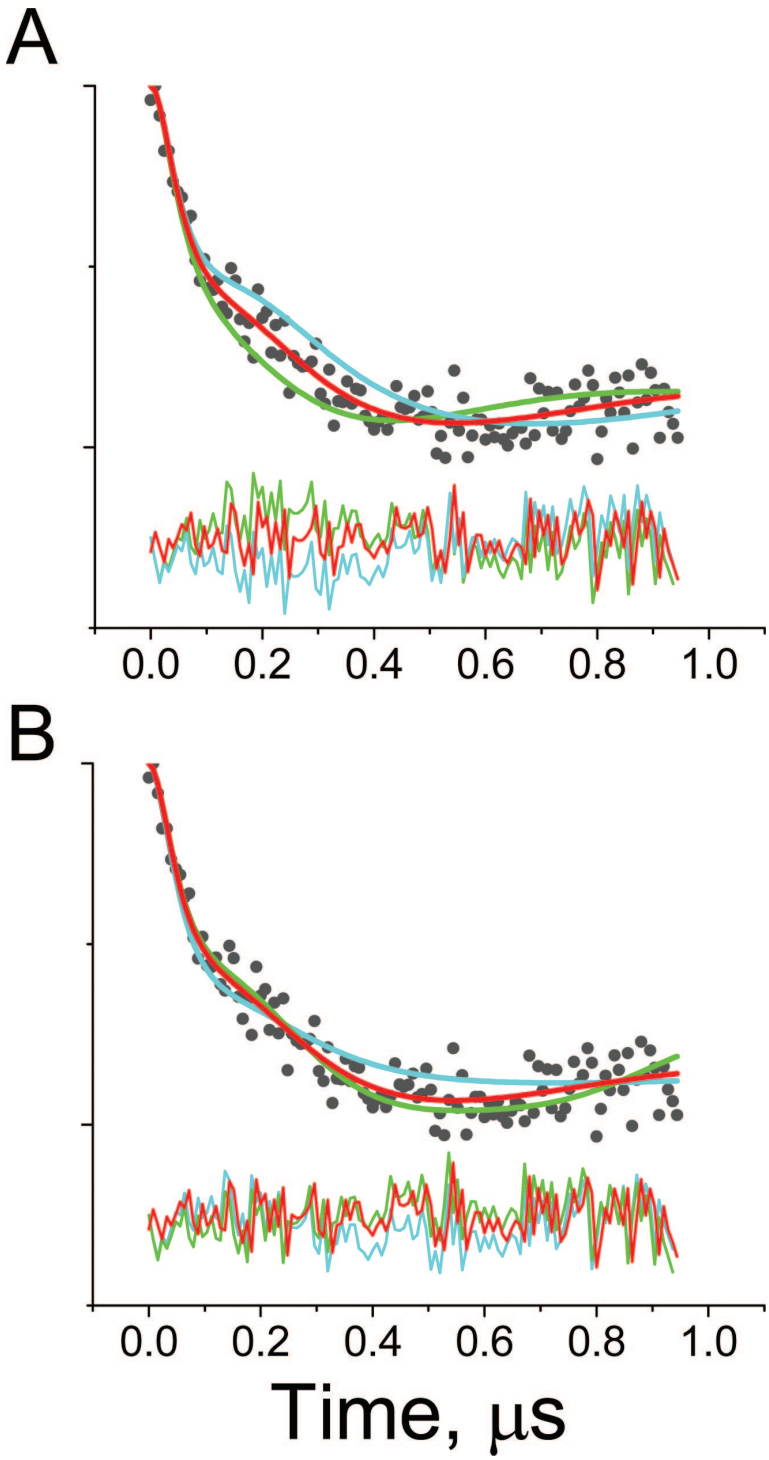

Fig. S3. Effect of varying DEER fitting parameters for 537:401 in the actin-bound state. Fitting parameters including the Gaussian distribution center (*A*) and width (*B*) for the long distance component were varied (parameters for the short distance component and the mole fraction were fixed). Residuals were calculated as experiment minus simulation. The best fit assuming two Gaussian distance distributions is shown in Table S2. (*A*) Simulated DEER decays and residuals based on distribution centers of 3.4 nm (dark green), 3.7 nm (red), and 4.0 nm (dark blue) are overlaid on the experimental DEER decay. Width of the distribution was fixed at 0.8 nm. (*B*) Simulated DEER decays and residuals based on distribution widths of 0 nm (green), 0.8 nm (red), and 1.8 nm (cyan) are overlaid on the experimental DEER decay. Center of the distribution was fixed at 3.7 nm.

Table S1. Functional properties of spin-labeled S1dC mutants

S1dC mutant	High salt Ca/K ATPase,* s^{-1}	Actin-activated ATPase,* s^{-1}	Fraction S1dC bound in rigor†	Labeling extent,‡ spins per head
Unlabeled A250C	7.2 ± 1.2	0.36 ± 0.04	1.0 ± 0.01	—
IPSL-G401C	6.8 ± 0.9	0.5 ± 0.01	1.0 ± 0.01	0.7 ± 0.1
IPSL-S416C	8.4 ± 1.4	2.1 ± 0.3	1.0 ± 0.01	0.3 ± 0.1
IPSL-K587C	1.8 ± 0.1	0.22 ± 0.04	0.82 ± 0.12	0.95 ± 0.2
IPSL-D583C	4.3 ± 0.2	2.9 ± 0.4	1.0 ± 0.01	1.2 ± 0.2
MSL-S416C, -D583C	3.3 ± 0.6	0.22 ± 0.02	1.0 ± 0.01	1.9 ± 0.2
MSL-F270C, -463C	2.9 ± 0.2	0.51 ± 0.06	0.85 ± 0.15	2.2 ± 0.2
IPSL-N537C, -S416C	6.0 ± 0.5	1.3 ± 0.3	1.0 ± 0.01	2.0 ± 0.3
IPSL-N537C, G401C	2.6 ± 0.2	0.2 ± 0.02	1.0 ± 0.01	1.9 ± 0.2
IPSL-N537C, -G366C	3.2 ± 0.1	0.8 ± 0.3	1.0 ± 0.01	2.0 ± 0.3

*Buffer conditions for ATPase and co-sedimentation assays are given in *SI Methods*.
†Fraction S1dC bound in rigor determined by co-sedimentation assay (28).
‡Extent of labeling determined by spin-counting.

Table S2. Fitting parameters for dipolar broadened CW EPR spectra

	One Gaussian			Two Gaussians						Three Gaussians								
Sample	r_1	w_1	RSS*	r_1	w_1	x_1	r_2	w_2	RSS*	r_1	w_1	x_1	r_2	w_2	x_2	r_3	w_3	RSS*
270:463																		
apo	0.9	1.5	1.0E-5	0.8	0.2	0.44	1.4	0.4	7.8E-6	0.8	0.2	0.41	1.2	0.3	0.35	2.2	0.3	5.7E-6
ADP·V	0.8	0.5	2.0E-5	0.8	0.2	0.88	2.2	0.3	7.1E-6	0.8	0.2	0.87	1.4	0.2	0.03	2.1	0.8	6.9E-6
actin	1.7	1.5	1.6E-5	0.8	0.2	0.31	2.2	0.3	1.0E-5	0.8	0.2	0.30	1.5	0.3	0.05	2.3	0.4	9.3E-6
416:583																		
apo	1.0	0.7	1.9E-3	0.8	0.2	0.43	1.1	0.2	1.6E-3	0.9	0.2	0.40	1.1	0.4	0.25	1.2	0.4	1.6E-3
ADP·V	1.1	0.2	1.8E-3	1.0	0.1	0.14	1.1	0.3	1.7E-3	1.0	0.1	0.14	1.1	0.3	—	—	—	1.7E-3
actin	1.1	0.7	1.4E-3	1.0	0.4	0.37	1.4	0.5	1.2E-3	0.9	0.3	0.29	1.2	0.4	0.29	1.3	0.5	1.1E-6

Simulated spectra were fit to experimental spectra (Fig 5) as described in *SI Methods*. Fitting parameters for $i = 1$, 2, or 3 Gaussian distance distributions are defined as follows: r_i is the center distance in nm, w_i is the full width half-maximum in nm, and x_i is the mole fraction. Shaded boxes indicate the fit that best represents the data based on RSS and residual plots (Fig. S2). Uncertainties were estimated from SD of repeated experiments ($n = 3$–5). For distances 0.8–2.0 nm, fractional uncertainties in r and w were ≈10% and 25%, respectively. For $r > 2$ nm, error estimates were not reliable.
*Residual sum of squares (RSS) is the sum of the squared residuals between the data and the simulated fit.

Table S3. Summary of spin-spin distance measurements in the outer cleft

	CW EPR		DEER						Structural models			
Sample	r_1	w_1	r_1	w_1	x_1	r_2	w_2	$\langle r\rangle_D$*	PDB	$r_{C\beta-C\beta}$†	$\langle r\rangle_{MDres}$‡	$\langle r\rangle_{MD}$‡
537:366												
apo	2.1	2.0	2.7	1.6	0.83	3.6	2.8	2.8	1FMV	2.2	1.8	3.0
ADP·V	2.1	2.0	2.4	0.9	0.48	3.1	1.4	2.7	1VOM	2.2	2.2	2.7
actin	2.1	2.0	2.3	1.2	0.89	3.9	1.2	2.5	1W8J	1.9	2.3	2.8
537:401												
apo	2.3	2.3	2.1	1.2	0.81	2.8	2.1	2.2	1FMV	1.3	1.3	1.2
ADP·V	2.5	2.2	2.2	1.4	0.89	2.9	2.1	2.3	1VOM	1.6	1.5	1.6
actin	2.0	2.0	2.2	0.7	0.47	3.7	0.8	3.0	1W8J	2.8	3.6	2.9
537:416												
apo	1.7	1.0	2.1	0.7	0.57	2.8	1.6	2.4	1FMV	1.8	0.7	1.7
ADP·V	1.7	1.0	1.9	0.7	0.33	2.4	0.8	2.3	1VOM	2.0	1.2	2.3
actin	1.6	1.0	1.9	0.9	0.70	2.6	1.9	2.1	1W8J	1.4	1.3	1.4

Simulated spectra were fit to experimental spectra as described in *SI Methods*. Fitting parameters for $i = 1$, 2, or 3 Gaussian distance distributions are defined as follows: r_i is the center distance in nm, w_i *is the full width half-maximum in nm, and* x_i is the mole fraction. Uncertainties were estimated from SD of repeated experiments ($n = 3$–5). For distances 1.6–3.0 nm, fractional uncertainties in r and w were ≈12%.

*$\langle r\rangle_D$ is the weighted average over distance distribution extracted from fit to DEER decay.

†Distances (in nanometers) between C^β ($r_{C\beta-C\beta}$) for the unlabeled residue. For Gly residues, C^α were used.

‡Weighted average over distance distribution for the restrained C^α MD simulation ($\langle r\rangle_{MDres}$) or unrestrained C^α MD simulation ($\langle r\rangle_{MD}$).

Table S4. Comparison of rigor-like structural models

			Rigor-like structural models			
	DEER		Myosin V (1W8J)		Myosin II (1Q5G)	
Site	$\langle r \rangle$*	$\langle r \rangle_{apo}$–$\langle r \rangle_{actin}$†	C^{β}–C^{β}‡	Δr§	C^{β}–C^{β}‡	Δr§
537:366	2.5	−0.3	1.9	−0.3	2.6	+0.4
537:401	2.2,3.7	0, +1.5	2.8	+1.5	2.6	+1.3
537:416	2.1	−0.3	1.4	−0.4	2.0	+0.2

*Weighted average of experimental DEER distance distribution, except for 537:401, where the two components are treated separately (separated by comma)
†Difference between $\langle r \rangle$ for the *apo* and actin-bound biochemical states
‡Distance between C^{β} (C^{α} substituted if Gly side chain)
§Difference between C^{β}–C^{β} distances for postrigor structure (1FMV) and rigor-like structure (1W8J or 1Q5G)